Molecular dissociation induced by electron transfer to multicharged ions

Folkerts, Hein Otto

Chapter 3

He^{2+} - He collisions: one-electron capture and target-ion excitation

By means of Photon Emission Spectroscopy we have studied state selective one-electron capture and target-ion excitation in collisions of He^{2+} with He. The collision energy has been varied from 1 to 75 keV/amu. Four-body Classical Trajectory Monte Carlo calculations have been performed by Meng and Olson in the energy range of 50 to 300 keV/amu. In the energy range where experiment and theory overlap there is in general fair agreement, although the l distributions within a principal quantum shell deviate from each other. At energies below 50 keV/amu the experiments confirm the results of Atomic Orbital calculations by Fritsch. For energies below 10 keV/amu we obtain the striking result that He^{+}(n=4) ions are formed with equal likelihood (i) in the projectile by one-electron transfer, and (ii) in the target by removing one of the target electrons and simultaneously exciting the residual ion. Combining all the experimental and theoretical data we have determined a reliable cross section data base for use in neutral helium beam based plasma diagnostics on large tokamaks.

3.1 Introduction

Charge eXchange Spectroscopy (CXS) has established itself as an important tool for magnetically confined nuclear fusion plasma diagnostics [27–29,8]. CXS based on visible light emission arising from electron capture from the injected neutral heating beams by plasma ions is a primary tool used to determine local plasma quantities such as ion temperatures and densities. Crucial for a reliable determination of plasma parameters is an accurate knowledge of the underlying state selective electron capture cross sections.

The recent introduction of neutral He beams at large tokamaks such as JET and the lack of state selective electron capture cross sections (Summers *et al.* 1991 [9]) has motivated the present work on the He^{2+}+ He collision system. He^{2+} ions are one of the major plasma impurities. Nowadays due to the injection of neutral helium, but also in plasmas containing D and T where alpha particles are the product of the thermonuclear fusion reaction.

Apart from this applied interest in He^{2+}+ He collisions there is a considerable fundamental interest in this collision system since, because of its intrinsic symmetry, it may be regarded as the simplest two-electron system in which one-electron capture processes can be studied. On the other hand, it is just this symmetry together with the large exo- or endothermicity of the different one-electron transfer channels that complicates a theoretical description of the system (see e.g. the paper by Fritsch (1994) [30]). Two-electron capture into the ground state of the projectile ion is a resonant process which at energies below $\sim$ 10 keV/amu exceeds one-electron capture (see e.g. Shah *et al.* [31]). One-electron capture can be regarded as being more or less a secondary process to two-electron capture into the ground state. Another illustration of the role of the symmetry in this system is described in this chapter. We will show that at energies below 10 keV/amu $He^+(n = 4)$ ions are produced with equal likelihood by processes of the following type:
(i) one-electron capture:

$$ {}_pHe^{2+} + {}_tHe(1s^2) \longrightarrow {}_pHe^{+}(n) + {}_tHe^{+}(1s) \quad (3.1) $$

and
(ii) capture into the ground state and simultaneous excitation of the target-ion:

$$ {}_pHe^{2+} + {}_tHe(1s^2) \longrightarrow {}_pHe^{+}(1s) + {}_tHe^{+}(n). \quad (3.2) $$

Likewise, at energies above $\sim$ 100 keV/amu excited target ions are produced by
(iii) single ionisation and simultaneous excitation of the target-ion:

$$ {}_pHe^{2+} + {}_tHe(1s^2) \longrightarrow {}_pHe^{2+} + {}_tHe^{+}(n) + e. \quad (3.3) $$

In equations (3.1-3.3) the subscripts p and t have been added to distinguish between the projectile and target particles. From now on process (i) will be referred to as electron capture and processes (ii) and (iii) as target-ion excitation.

In this chapter we present experimental data for HeII($n = 4 \rightarrow n = 3$) line emission by projectile or target $He^+(4l)$ ions, and also the separate

$He^{+}(4l)$ one-electron capture cross sections, process (i). Furthermore results for HeII($np \rightarrow 1s$) Lyman emission are presented. This large set of data, covering impact energies from 1.5 to 75 keV/amu, allows us to make a detailed comparison with Classical Trajectory Monte Carlo (CTMC) calculations (50 to 300 keV/amu) presented here and Atomic Orbital (AO) calculations (4 to 65 keV/amu) by Fritsch [30]. From this comparison it is possible to deduce a recommended cross section data set with which future theoretical and experimental data may be compared and which can be used as input for CXS modelling of fusion plasmas.

3.2 Experiment

3.2.1 Experimental set-up

Details of the experimental set-up are discussed in chapter 2. Here only the most important points will be summarised.

He^{2+} ions are extracted from the ECR ion source with energies of 1 to 13 keV/amu. To obtain experimental data at energies encompassing the 30 to 55 keV/amu injection energy of the He beams at JET we have used the post-accelerator to boost the energies of our beams up to 75 keV/amu.

In the set-up for photon emission spectroscopy the ions cross an atomic He-beam target which has a full width at half maximum of 4 mm. The HeII($n = 4 \longrightarrow n = 3$) emission at 468.6 nm is observed perpendicular to the ion beam with a spectrometer for visible light. This spectrometer is equipped with an imaging system that allows for scanning along the ion beam. This is essential for determining the HeII($n = 4 \longrightarrow n = 3$) cross sections accurately, and is used to determine the different HeII($4l \rightarrow 3l'$) transitions contributing to the HeII($n = 4 \rightarrow n = 3$) line emission as discussed in the next section.

The HeII($np \rightarrow 1s$) Lyman transitions, having wavelengths in the range of 24.0 to 30.4 nm, are measured with a grazing incidence VUV monochromator. A position sensitive microchannel plate detector enables the simultaneous detection of all the HeII Lyman lines.

3.2.2 Deconvolution of the emission profiles

As discussed in section 2.2.2 we can exploit the fact that the lifetimes of the $He^{+}(4l)$ projectile states are so long that a considerable fraction of the ions decays downstream from the atomic target along the ion beam. Figure 3.1 shows as an example the spatial HeII($n = 4 \rightarrow n = 3$) emission profile for 4.5 keV/amu He^{2+} ions colliding with He. Such a measured emission profile can not be fitted by the emission profiles corresponding only to the four $He^{+}(4l)$ projectile states. Note that already at this relatively low impact energy the maxima of these profiles, indicated in figure 3.1 by the thin full curves, are shifted downstream and so they can never reproduce the measured profile which exhibits a maximum at $z = 0$, coinciding with the target centre. This clearly indicates that for the symmetric He^{2+} + He system we need a fifth component describing the excited $He^{+}(4l)$ target ions, produced via process (ii). Since the velocity of the target particles is negligibly small,

the spatial emission profiles of all $He^+(4l)$ target-ion states reduce to the target profile, T(z) (eq. (2.2) with v approaching 0).

While the magnitudes of the separate electron capture fits turn out to be sensitive to the exact shape of the neutral He target beam profile, the sum is insensitive. Therefore the ratio R_{43} of the target-ion excitation and electron capture components of the observed HeII($n = 4 \rightarrow n = 3$) emission can be determined rather accurately. Considering the $He^+(4l)$ one-electron capture components, deduced from a five-parameter fit, it is especially the $4p$ that scatters severely. This is mainly due to its small contribution to the HeII($n = 4 \rightarrow n = 3$) transition (branching ratio of only 4%, see figure 2.3). Note that in principle the cross section, $\sigma_{cap}(4p)$, for capture into $He^+(4p)$ can be determined from the HeII($4p \rightarrow 1s$) transition in the VUV. In collisions of He^{2+} on H and Li [18,20], Hoekstra *et al.* indeed used $\sigma_{cap}(4p)$ determined from its VUV emission to improve the quality of the fit by subtracting the small contribution of the $4p$ state from the HeII($n = 4 \rightarrow n = 3$) signals to reduce the number of fit parameters by one. For the present symmetric He^{2+}+ He system it is more complicated because we have to consider that also target-ion excitation is contributing to the VUV transition, and moreover that at the highest impact energies a fraction of the $He^+(4p)$ projectile ions decays outside the observation region of the VUV spectrometer. Nevertheless it is possible to determine $\sigma_{cap}(4p)$ in an approximate manner from the VUV transition. The relation between the capture, $\sigma_{cap}(4p)$, the target-ion excitation, $\sigma_{exc}(4p)$ and the apparent emission cross section,

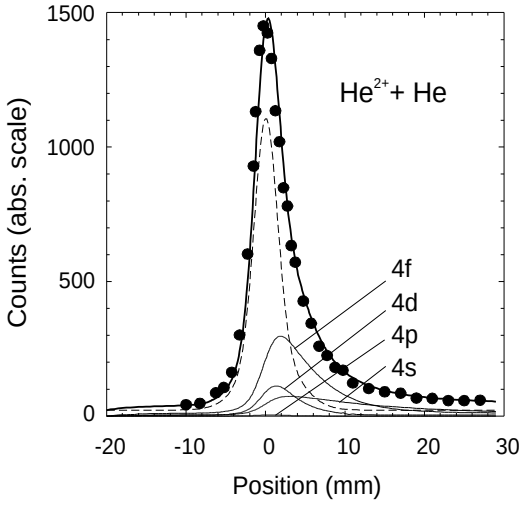

Figure 3.1: *Spatial HeII($n=4 \rightarrow n=3$) emission profile for 4.5 keV/amu He^{2+} ions colliding on He. The separate 4l electron capture (process (i)) contributions and the target-ion excitation (processes (ii) and (iii)) contribution are indicated respectively by the thin full curves and the broken curve. The component due to capture into HeII(4p) state is hardly observable above the horizontal axis, because of its small $4p \rightarrow nl$ branching ratio of only 4%, cf. figure 2.3.*

$\sigma_a(4p \rightarrow 1s)$ is given by:

$$\sigma_a(4p \rightarrow 1s) = \beta(4p \rightarrow 1s) * [\sigma_{exc}(4p) + F_{obs}\sigma_{cap}(4p)] \quad (3.4)$$

with $\beta(4p \rightarrow 1s)$ the branching ratio for the HeII($4p \rightarrow 1s$) transition, i.e. 0.84, and F_{obs} the fraction of the $He^+(4p)$ projectile ions for which the decay is observed by the VUV spectrometer. This fraction is given by:

$$F_{obs} = \int_{-L}^{L} P_{4p}(z)dz \; / \; \int_{-L}^{L} T(z)dz \quad (3.5)$$

with $P_{4p}(z)$ as given in equation (2.2), T(z) the target beam profile and 2L the observation length of the VUV spectrometer, 7.5 mm. For projectile ions in the $4p$ state F_{obs} is calculated to change from 1 at energies $\leq$ 20 keV/amu, to almost 0.7 at the highest energy of 75 keV/amu. For the $2p$ and the $3p$ state F_{obs} remains equal to 1 over the whole energy range, due to their shorter lifetimes.

We used the following procedure to determine the $4p$ one-electron capture cross section. First we calculated the ratio $R_{43} = (\sigma_{exc}(4 \rightarrow 3) \; / \; \sigma_{cap}(4 \rightarrow 3))$ by performing a five-parameter fit to the HeII($n = 4 \rightarrow n = 3$) emission profiles. Then we assumed that the excitation/capture ratio for the $4p$ state is equal to R_{43}. In that way equation (3.4) reduces to

$$\sigma_a(4p \rightarrow 1s) = \beta(4p \rightarrow 1s)\sigma_{cap}(4p)[R_{43} + F_{obs}]. \quad (3.6)$$

With $\sigma_{cap}(4p)$ determined from the equation above as an input parameter, the HeII($n = 4 \rightarrow n = 3$) emission profile was fitted again. The whole procedure was repeated with the new but only slightly modified ratio R_{43}.

3.2.3 Experimental results and error discussion

The experimental HeII($np \rightarrow 1s$) emission cross sections are given in table 3.1, together with their relative uncertainties. It is to be realised that these cross sections include contributions of one-electron capture, process (i), as well as contributions of target-ion excitation, processes (ii) and (iii). At energies larger than 20 keV/amu the HeII($4p \rightarrow 1s$) emission cross sections have been corrected for the loss of intensity described by F_{obs}. Following equation (3.6) the correction factor, $(1 + R_{43}) \; / \; (F_{obs} + R_{43})$, is found to change from 1 at the lower energies to approximately 1.35 at the highest impact energy, 75 keV/amu.

At the wavelengths of the HeII($np \rightarrow 1s$) lines the systematic absolute calibration error is approximately 20% [18]. The relative errors in the cross sections are the quadratic sum of the statistical error at 90% confidence level, a possible fluctuation in the overlap of the ion and target beam and a possible contribution due to capture from the residual background gas. To check the latter effect some measurements have been performed with no He target present. They indicate that capture from background gas contributes much less than 5% to measured signals. From the day-to-day reproducibility of the cross sections for the most intense line, HeII($2p \rightarrow 1s$), for which the uncertainty in the counting statistics is small, we estimate the uncertainty in the

overlap of the beams to be 5 and 10% for direct and post-accelerated beams, respectively.

For the HeII($n = 4 \rightarrow n = 3$) emission cross sections, given in table 3.2 together with their one-electron capture and target-ion excitation components, the absolute error is 20%. Although this photon detection system is not positioned at the double magic geometry the error due to neglecting polarisation effects is estimated to be less than 5% at the wavelength of 468.6 nm [18]. For the separated target-ion excitation and capture cross sections the relative errors are due to the same sources as for the VUV lines plus the uncertainty of the fit procedure. Especially for the $He^+(4l)$ electron capture cross sections, presented in table 3.3, the latter errors are dominating. These "fitting" errors are deduced from the variation of the $He^+(4l)$ electron capture cross sections with changing the target beam profile (within the experimental error bars) and by letting the ratio factor for $4p$ deviate from R_{43}, see previous section. The errors found in this way are much larger than the ones which can be calculated from the diagonal elements of the inverted least squares matrix.

Finally some measurements where repeated with isotopic $^3He^{2+}$ to verify that impurity ions with the same charge-to-mass-ratio as $^4He^{2+}$, C^{6+} and especially H_2^+ do not influence the measurements.

Table 3.1: *He^{2+} + He: Experimental HeII ($np \rightarrow 1s$) emission cross sections and relative errors (in 10^{-18} cm^2) versus impact energy E (in keV/amu). The data include one-electron capture and target-ion excitation.*

	$2p \rightarrow 1s$		$3p \rightarrow 1s$		$4p \rightarrow 1s$	
E	σ_{em}	$\Delta\sigma_{em}$	σ_{em}	$\Delta\sigma_{em}$	σ_{em}	$\Delta\sigma_{em}$
1.5	37	7.5	2.4	0.7		
2	36	6.5	3.1	0.65		
2.5	36	5.5	3.3	0.6		
3.5	44	5.0	3.8	0.6	0.31	0.25
4.5	45	4.5	3.5	0.6	0.46	0.30
6	48	4.5	3.4	0.5	0.54	0.30
8	50	4.5	2.9	0.45	0.70	0.24
9	52	4.5	2.5	0.5	0.72	0.22
11	66	6.0	3.9	0.6	0.92	0.26
13	78	6.5	4.5	0.65	0.96	0.29
20	83	17	4.8	1.1	1.17	0.42
27.5	142	30	9.1	2.0	1.94	0.65
30	114	16	8.8	1.8	2.1	0.55
40	112	11	10.1	1.8	2.3	0.65
45	104	10	12.5	1.8	3.3	0.75
47.5	109	11	14.2	1.9	3.7	0.85
50	119	13	15.0	1.9	2.9	0.85
52.5	102	11	14.1	1.9	3.5	0.9
60	83	10	12.6	2.0	2.5	1.1
70	94	13	16.3	2.2	3.2	1.2
75.5	65	11	14.0	1.9	2.8	1.3

Table 3.2: *He^{2+} + He: Experimental HeII (n=4 → n=3) emission cross sections and relative errors (in 10^{-18} cm^2) versus impact energy E (in keV/amu). The columns present from left to right the total emission cross sections and the contributions due to respectively one-electron capture (process (i)) and target-ion excitation (processes (ii) and (iii)).*

	total		one-electron capture		target-ion excitation	
E	σ_{em}	$\Delta\sigma_{em}$	σ_{em}	$\Delta\sigma_{em}$	σ_{em}	$\Delta\sigma_{em}$
1.5	1.0	0.15	0.52	0.11	0.48	0.11
2	0.91	0.15	0.42	0.11	0.49	0.11
2.5	1.1	0.15	0.54	0.12	0.56	0.12
3.5	0.83	0.15	0.42	0.12	0.41	0.12
4.5	1.05	0.15	0.54	0.12	0.51	0.12
6	1.01	0.14	0.48	0.1	0.53	0.1
8	1.01	0.13	0.52	0.1	0.49	0.1
9	1.06	0.12	0.60	0.1	0.46	0.1
11	1.31	0.15	0.76	0.12	0.55	0.11
13	1.39	0.15	0.80	0.13	0.59	0.11
20	1.83	0.25	1.04	0.20	0.79	0.20
30	2.29	0.25	1.76	0.20	0.53	0.12
40	2.58	0.25	2.16	0.20	0.42	0.10
50	2.46	0.25	2.09	0.20	0.33	0.10
60	2.47	0.25	2.17	0.20	0.26	0.09
70	2.55	0.30	2.12	0.25	0.35	0.11
75.5	2.25	0.30	1.97	0.25	0.28	0.10

Table 3.3: *He^{2+} + He: Experimental $He^{+}(4l)$ one-electron capture cross sections and their relative errors (in $10^{-18}cm^2$) versus impact energy E (in keV/amu).*

E	$\sigma(4s)$	$\Delta\sigma(4s)$	$\sigma(4p)$	$\Delta\sigma(4p)$	$\sigma(4d)$	$\Delta\sigma(4d)$	$\sigma(4f)$	$\Delta\sigma(4f)$
1.5	0.45	0.25	0.07	0.04	0.12	0.06	0.25	0.12
2	0.30	0.15	0.09	0.05	0.14	0.07	0.21	0.11
2.5	0.35	0.16	0.11	0.05	0.14	0.07	0.20	0.10
3.5	0.40	0.20	0.15	0.07	0.24	0.12	0.23	0.12
4.5	0.30	0.18	0.29	0.10	0.30	0.15	0.25	0.12
6	0.30	0.15	0.34	0.11	0.30	0.15	0.25	0.12
8	0.23	0.12	0.45	0.14	0.48	0.20	0.35	0.15
9	0.19	0.10	0.48	0.15	0.50	0.20	0.31	0.11
11	0.21	0.10	0.65	0.19	0.98	0.40	0.40	0.17
13	0.21	0.10	0.83	0.25	1.10	0.50	0.40	0.18
20	0.45	0.25	0.90	0.45	1.30	0.60	0.45	0.23
30	1.50	0.60	1.63	0.65	0.96	0.44	0.60	0.25
40	2.0	0.8	2.5	1.0	1.1	0.5	0.60	0.25
50	2.3	0.7	2.9	1.4	1.9	0.7	0.5	0.2
60	2.1	0.7	2.6	1.3	2.1	0.7	0.5	0.2
70	2.3	0.7	3.6	1.7	2.2	0.7	0.45	0.2
75.5	2.0	0.7	2.9	1.5	1.6	0.7	0.4	0.2

3.3 CTMC calculations

At energies between 50 and 300 keV/amu Classical Trajectory Monte Carlo (CTMC) calculations were performed by Meng and Olson. In the CTMC method both He target electrons were incorporated in a 4-body, 3-dimensional calculation (Meng *et al.* 1993 [32]). The initialisation of the electron orbits was obtained by using a model potential derived by Clementi and Roetti (1974) [33]. In order to incorporate radial correlation between the electrons, the screening parameters of the electrons were varied during the collision according to their respective binding energies to the target nucleus using a procedure developed by Montemayor and Schiwietz [34]. In such a method the energies required to ionise, capture or excite one or both electrons for reactions (i), (ii) and (iii) closely reproduce the true values.

In this method the interactions between the four particles involved in the collision, namely, the projectile, the target nucleus and the two target electrons are described exactly by the sum of the two-body Coulomb interactions. Taking M for the equal masses of the He target and projectile and m for the electronic mass, the Hamiltonian of the collision system has the form:

$$H = \frac{p_t^2 + p_p^2}{2M} + \frac{p_1^2 + p_2^2}{2m} + \frac{Z_p Z_t}{|r_p - r_t|} - \frac{Z_p}{|r_1 - r_p|} - \frac{Z_p}{|r_2 - r_p|} - \frac{Z_t}{|r_1 - r_t|} - \frac{Z_t}{|r_2 - r_t|} + V_{12}(r_1, r_2) \tag{3.7}$$

where p_p, p_t, p_i, r_p, r_t and r_i, i = 1, 2, are the momenta and coordinates of the projectile, the target nucleus and the electrons, respectively. The charge states of the projectile and the target nucleus are Z_p and Z_t, respectively. For the He^{2+}+ He system $Z_p = Z_t = 2$. The Coulomb potential between the two electrons, $V_{12}(r_1, r_2)$, can be approximated by the sum of the potentials of each individual electron due to the screening of the target nucleus by the other electron,

$$V_{12}(r_1, r_2) = V_1(r_1) + V_2(r_2) \tag{3.8}$$

where $V_1(r_1)$ and $V_2(r_2)$ are given by:

$$V_1(r_1) = \frac{1 - (1 + \lambda_2 |r_1 - r_t|) exp(-2\lambda_2 |r_1 - r_t|)}{|r_1 - r_t|} \tag{3.9}$$

and

$$V_2(r_2) = \frac{1 - (1 + \lambda_1 |r_2 - r_t|) exp(-2\lambda_1 |r_2 - r_t|)}{|r_2 - r_t|}. \tag{3.10}$$

In equations (3.9) and (3.10), λ_1 and λ_2 represent the screening of the He-target nucleus by electrons 1 and 2, respectively.

Substituting the above given forms of the Coulomb potential between the two electrons into the Hamiltonian (eq. (3.7)) gives the model potential Hamiltonian that is used for the description of the He^{2+}+ He system. Initially, the potential parameters λ_1 and λ_2 are set equal and taken to be 1.6875. This value, λ_{1s}, is given by variational calculations of the ground state binding energy of the helium atom. During the course of the collision, the values of λ_1 and λ_2 are varied

linearly with effective binding energy, E_j, $j = 1$, 2 of electron 1 and 2 as follows [34]:

$$\lambda_j = \begin{cases} 0 & \text{for } E_j > 0 \\ \frac{\lambda_{1s}}{E_{1s}} E_j & \text{for } E_{1s} < E_j \leq 0 \\ \lambda_{1s} & \text{for } E_j \leq E_{1s} \end{cases} \quad (3.11)$$

By varying the screening parameters λ_1 and λ_2, when one electron is ionised, the other electron will be bound more tightly to the nucleus than prior to the collision. The initial binding energy, E_{1s} of each electron on He, takes the value of 0.896.

After the trajectories have been integrated and final binding energies between all interacting particles have been determined, electron capture and ionisation events are identified. The energy and angular momentum of each captured electron relative to the He^{2+} core is then used to determine its nl value using semi-quantal binning criteria described by Olson [35]. A classical principal quantum number n_c is obtained from the binding energy U of the electron by

$$U = \frac{-Z^2}{2n_c^2} \quad (3.12)$$

where $Z = Z_p = Z_t$ is the charge of the core. Then, n_c is related to the quantum number n of the final state by the condition [36]

$$\left[(n-1)(n-\frac{1}{2})n\right]^{\frac{1}{3}} \leq n_c \leq \left[n(n+\frac{1}{2})(n+1)\right]^{\frac{1}{3}}. \quad (3.13)$$

The normalised classical angular momentum is defined as $l_c = (n/n_c)(\vec{r}+\vec{p})$, where $\vec{r}$ and $\vec{p}$ denote the position and momentum vectors of the electron relative to the core. l_c is related to the orbital quantum number l of the final state by

$$l \leq l_c \leq l+1. \quad (3.14)$$

Given the number of trajectories that lead to a specific nl level of He^+, the cross section in atomic units is then calculated by

$$\sigma = \pi b_{max}^2 \frac{N(n,l)}{N_{tot}} \quad (3.15)$$

where $N(n,l)$ denotes the number of events that lead to the nl level and N_{tot} is the total number of trajectories integrated. b_{max} is the impact parameter beyond which the probability of electron capture or ionisation is negligibly small.

Calculations made using this method indicate that two-electron processes (process (iii)) make an important contribution to the line emission cross sections at the higher energies studied by the CTMC method.

3.4 Discussion

The HeII($np \rightarrow 1s$) emission cross sections are shown in figure 3.2 in which they are compared with the results of the atomic-orbital (AO) calculations [30] and the CTMC results. The AO data predict the general trends in the data well, especially noteworthy is the dip in the HeII($3p \rightarrow 1s$) emission cross section at approximately 8 keV/amu. The CTMC results have only a small overlap in energy range with our experimental

data. At this 50 to 75 keV/amu range there is a rather good agreement which makes the CTMC cross sections for these transitions a reliable extension of the experimental ones to higher impact energies.

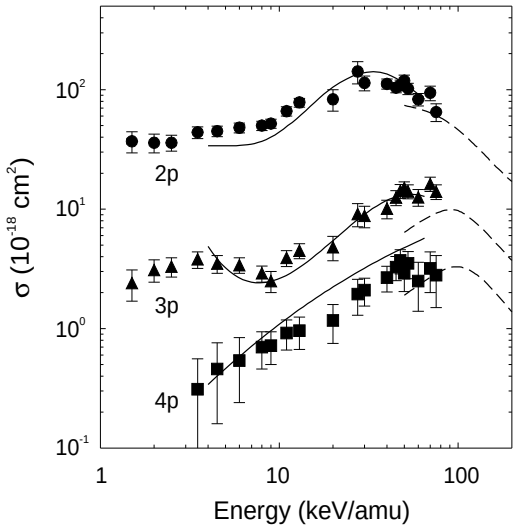

Figure 3.2: *Line emission cross sections for HeII($np \rightarrow 1s$). The symbols are indicating our experimental results. Only relative errors are shown. Theoretical curves: broken curves, CTMC calculations: presented here; full curves, AO calculations: Fritsch [30].*

In figure 3.3 the HeII($n = 4 \rightarrow n = 3$) total emission cross sections are shown together with the separate contributions resulting from electron capture (process (i)) and target-ion excitation (processes (ii) and (iii)). The AO calculations are in general agreement with the experiments. The structure in the AO results is probably an artifact caused by the fact that the $n = 4$ states feeding the HeII($n = 4 \rightarrow n = 3$) transition are the highest levels included in the basis set. For a more detailed discussion see Fritsch [30]. For the total emission cross section the AO and CTMC results present the same trend as our experimental data, although the first overestimates and the second underestimates the experimental results. Both calculations as well as the experiments show a maximum around 60 keV/amu.

The most striking observation from this figure is that at energies below 10 keV/amu the cross sections for target-ion excitation are equal to the ones for electron capture. This is more clearly seen in figure 3.4 where the ratio of these processes is displayed. As will be discussed in the following sections it is expected that the ratio of target-ion excitation and electron capture is similar for states with $n \geq 3$. Since the calculations for capture to the $He^+(n = 4)$ states are less reliable than for capture to the $He^+(n = 3)$ states, in figure 3.4 we have plotted the AO cross section ratio for the population of $n = 3$ states instead, which is found to agree very well with the measured ratio for the $n = 4$ states. The AO calculations show that at these energies the electron removal accompanying target-ion excitation is due to electron transfer into the ground state of the He^{2+} projectiles.

The observation that below 10 keV/amu the probability for target-ion excitation and electron capture seem to be more or less equal is actually what one would expect from an argument based on the quasi-molecular behaviour of this symmet-

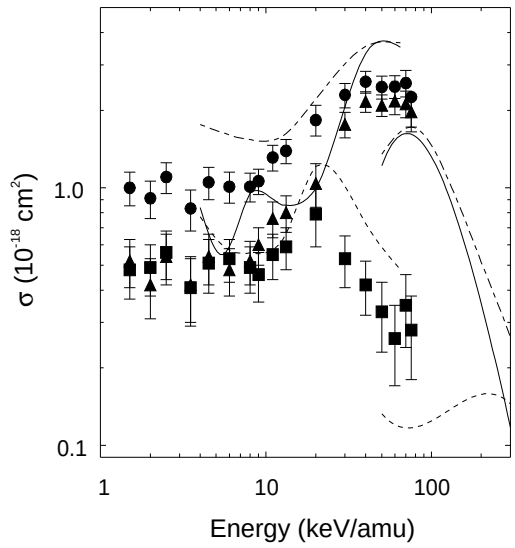

Figure 3.3: *The total line emission cross sections for HeII(n=4 → n=3) emission are indicated by the circles and chain curves. The separate contributions to this curve are indicated by triangles and full curves, electron capture (process (i)), and squares and broken curves, target-ion excitation (processes (ii) and (iii)). The symbols mark our experimental data. The curves display the theoretical results: from 4 to 65 keV/amu AO results of Fritsch [30] and above 50 keV/amu the CTMC results.*

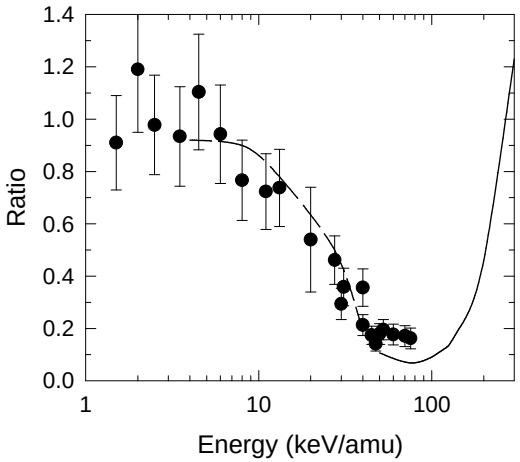

Figure 3.4: *Ratio of simultaneous electron removal and target-ion excitation cross sections (processes (ii) and (iii)) and one-electron capture (process (i)) cross sections as a function of impact energy. Experiment and CTMC calculation (full curve) are for HeII(n=4 → n=3) line emission. The broken curve denotes results of the AO calculation for the ratio of HeII (n=3) production.*

ric collision system. At large inter-atomic separations, the initial ^1S ground state of both the target and the projectile atoms can be visualised as superpositions of two molecular configurations, a *gerade* and an *ungerade* configuration with respect to interchange of the atomic centres. Both atomic states are formed by the two molecular configurations with equal absolute weight but different relative sign. With decreasing inter-atomic separation, the energy of the *gerade* $1S\Sigma_g$ configuration decreases sharply, it is associated with the lowest-energy curve in a molecular-energy diagram. On the other hand, the energy curve of the *ungerade* configuration would develop closer to the energies of other curves of the system. It is hence the configuration with *ungerade* symmetry which, in slow collisions, predominately leads to couplings to other states of the system. The eventually resulting atomic states can again be expressed as superpositions of *gerade* and *ungerade* molecular configurations. If then these states are primarily excited through their respective *ungerade* component it is clear that in the He atom or ion, excited states with the same atomic (ionic) configuration are nearly equally excited in target and projectile, through the same *ungerade* component. Any difference in the population would come from the *gerade* component which enters with different relative sign in the target and projectile atomic configurations, but this component is very weak in slow collisions (except of course in the initial and the resonant two-electron transfer channel [37]).

It is also possible to visualise the equal cross sections for electron capture into $n = 4$ and target-ion excitation into $n = 4$ in the framework of the classical overbarrier model (Niehaus 1986 [13]). This model assumes that on the way-in of the collision the He target electrons become subsequently molecular. On the way-out first the most tightly bound electron is captured by either the target or projectile nucleus. Since both particles are identical it is equally likely that this electron stays with the target or goes to the projectile. Now the weaker bound electron moves in the field of a 2+ and 1+ He ion. Although the probabilities for going to the singly or doubly charged ion are different, they do not depend on the fact whether it is the target or the projectile ion that is one- or two-fold charged. So it can intuitively be understood that target-ion excitation and electron capture are equally strong as long as collisions are considered in which both electrons become molecular. This has two implications which both agree with the prediction of the aforementioned molecular picture. Firstly, the one-electron capture and target-ion excitation processes are parasitic to two-electron capture processes, which are known to dominate at the lower impact energies [31]. This can be understood from the fact that at infinity the pure one-electron capture channels are by no means resonant, but those nearest to the entrance channel are exo- and endothermic by approximately 30 eV and 10 eV for $He^+(n = 1)$ and $He^+(n = 2)$, respectively. Secondly, for target-ion excitation the electron removed from the target is captured into the ground state of the projectile. That the general trend of the results at lower energies can be understood within the framework of the classical overbarrier model is surprising because the model assumes the electrons to be distinguishable, which for He is questionable.

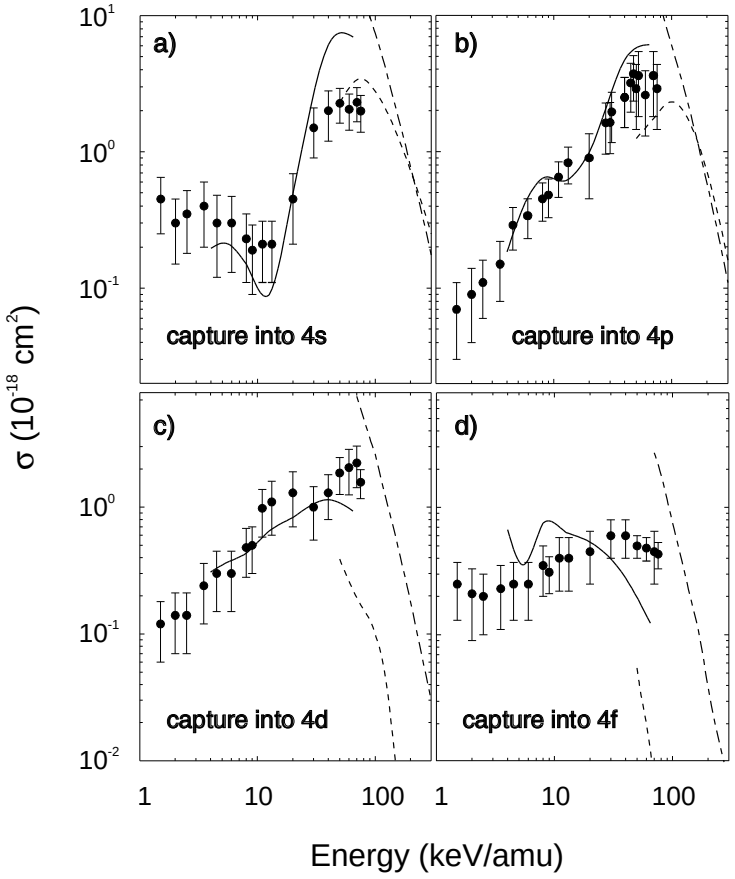

Figure 3.5: *State selective $He^+(4l)$ electron capture cross sections.* **a)** *4s*, **b)** *4p*, **c)** *4d and* **d)** *4f. The circles mark the present experimental results. Only relative errors are shown. Theoretical curves: full curves, AO: Fritsch [30]; broken curves, CTMC: presented here; chain curves, CDWA: Gayet et al. [38].*

The state selective $He^+(4l)$ electron capture cross sections, deduced from the spatial HeII($n = 4 \rightarrow n = 3$) signals and the well known branching ratios, are shown in figure 3.5 together with the various theoretical results, among which the cross sections from the Continuous Distorted Wave Approximation (CDWA) calculations of Gayet *et al.* (1993) [38]. From the comparison of similar CDWA calculations of Belkič *et al.* [39] with experimental data of Frieling *et al.* [53] for He^{2+} colliding with atomic hydrogen, we estimate that the CDWA results become reliable at energies exceeding 150 keV/amu. The AO cross sections agree fairly well with the experimental results, but the CTMC calculations predict far too low a population of the high l states. Sensitivity tests performed with different He model potentials were only able to confirm the convergence of the $4s$ and $4p$ capture cross sections at energies above 150 keV/amu. At these energies the $4d$ and $4f$ CTMC cross sections were found to be more than two orders of magnitude smaller than the dominant $4s$ and $4p$ channels. It is noteworthy that also the CDWA calculations predict $4d$ and $4f$ electron capture cross sections which are negligibly small with respect to the cross sections for capture into $4s$ and $4p$.

Although for capture into the $4s$ state the AO data seem to confirm the minimum in our results near 10 keV/amu, the increase of the measured cross section at energies below this value is probably an artifact. Such an effect has also been observed for the He^{2+}+ Li system [20]) and is inherent to our deconvolution method based on the lifetimes of the states. Because the lifetime of the $5g$ state is comparable to the lifetime of the $4s$ state (cf. figure 2.3), the depopulation of $5g$ via the $5g$ - $4f$ - $3d$ Yrast cascade is in the deconvolution procedure ascribed to the $4s$ state. As will be explained in the following section the $5g$ cascade contribution becomes significant at energies below $\sim$ 8 keV/amu. Due to the small branching ratios of the other ($5l \rightarrow 4l'$) transitions the ($5g \rightarrow 4f$) is the only one that has to be taken into account.

3.5 Recommended data for plasma diagnostics

The HeII($n = 4 \rightarrow n = 3$) line emission is usually exploited to determine the density and temperature of He ions in a tokamak plasma. Basically this transition is used because it lies in the visible spectral range. Its light can thus be transported by fiber optics to spectrometers installed at a large distance from the plasma vessel by which the background signals can be reduced. The HeII($n = 4 \rightarrow n = 3$) data of our crossed-beam experiments and calculations cannot be applied directly to plasma diagnostics since within the plasma the $He^+(4l)$ populations are redistributed. The redistribution, due to electric fields and collisions with other particles, leads to a nearly statistical population of the states within the $n = 4$ shell, with the possible exception of the lowest temperature and density regimes [28,29,41]. Therefore, at the larger tokamaks the conditions are such that knowledge of the total cross section for capture into the $He^+(4l)$ states, $\sigma(n = 4)$, suffices for plasma modelling purposes.

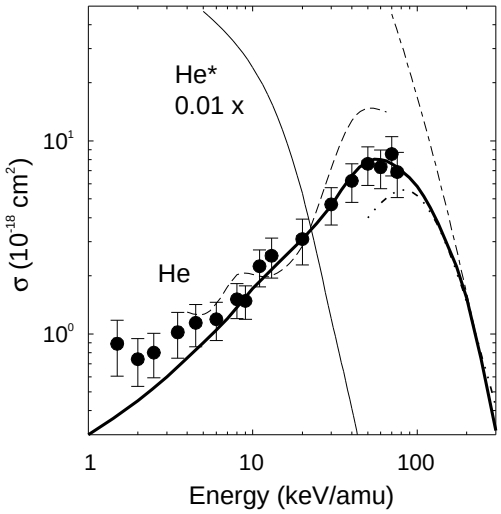

Figure 3.6: *State selective $He^+(n=4)$ electron capture cross sections in He^{2+} + He collisions. The circles mark the present experimental results. Only relative errors are shown. Theoretical curves: broken curves, AO: Fritsch [30]; double chain, CTMC: presented here; chain curve, CDWA: Gayet et al. [38]. The full curve shows the recommended cross sections. The thin full curve displays the CTMC $He^+(n=4)$ cross sections (multiplied by 0.01) in collisions of He^{2+} ions on metastable He(1s2s) atoms.*

The $n = 4$ cross section is obtained from our data by summing the state selective $He^+(4l)$ electron capture cross sections presented in figure 3.5 and table 3.3. Figure 3.6 displays $\sigma(n = 4)$ together with the theoretical predictions. The thick solid curve indicates the cross sectional behaviour we recommend for data base purposes. Numerical values are given in table 3.4. From high to low impact energies this recommended curve first follows the CDWA to around 200 keV/amu after which the CTMC results are followed to some 100 keV/amu. Then an interpolation is made to our experimental results, which are the basis for the recommended cross sections at energies below 75 keV/amu. At approximately 8 keV/amu the recommended curve starts to deviate from the experimental $\sigma(n = 4)$ because, as mentioned in the previous section, at these low energies there is an apparent $5g$-cascade contribution to the $4s$ cross section.

Since at low collision energies the population of the $4l$ states with $l \geq 1$ is nearly statistical it seems logical to assume that also the $4s$ state is populated according to its statistical weight. In doing so we find that the $5g$ contribution to the apparent $4s$ cross section must be significant and at the lowest energies (E $\leq$ 5 keV/amu) even exceeds the actual contribution of $4s$ by a factor of 3 to 5. In the following we will show that the assumption of a statistical population of the l states within an n shell yields a consistent picture. Besides a statistical population we assume a $(n/(n+1))^\alpha$ scaling to connect the different n shells. The scaling power α is determined from the cross section ratio of the HeII($3p \rightarrow 1s$) and HeII($4p \rightarrow 1s$) line emission. We find a scaling

Table 3.4: *He^{2+} + He: Recommended total cross sections for one-electron capture into He^+(n=4) (in 10^{-18} cm^2) versus impact energy E (in keV/amu).*

E	σ_{cap}	E	σ_{cap}	E	σ_{cap}
1	0.3	30	4.62	100	5.8
2	0.45	40	6.6	120	4.5
3	0.6	50	7.8	150	3
5	0.9	60	8	200	1.54
7	1.2	70	7.6	300	0.315
10	1.72	80	7	400	0.096
20	3.1	90	6.4	500	0.036

power of approximately 5. Using this scaling for the $5g$ state to correct the apparent $4s$ capture cross section, we find for example at a collision energy of 4.5 keV/amu a decrease of the cross section for capture into $4s$ by a factor 5. This yields a cross section of 6.5×10^{-20} cm^2, a value which is in agreement with the previously made assumption of a statistical $He^+(4l)$ population. At higher energies the relative population of the higher l states decreases and the contribution of the $5g$ cascade to the $4s$ capture cross section vanishes.

Besides $\sigma(n = 4)$ for He^{2+}+ He collisions, figure 3.6 includes also the CTMC $\sigma(n = 4)$ results for He^{2+} ions colliding on metastable He. The CTMC calculations have been performed with a one-electron model potential in a way similar to the calculations for multiply charged ions colliding on Li (Olson *et al.* [43]). Calculations were done both for singlet and triplet metastable He($1s2s$) atoms. The curve shown in figure 3.6 is the average of the cross sections for capture from the singlet and triplet metastables. At energies below approximately 15 keV/amu the singlet cross section is somewhat larger than the triplet one, while at higher energies the situation is reversed. This is due to the slightly smaller ionisation potential of the singlets.

The effect of the ionisation potential is clearer from the comparison of $\sigma(n = 4)$ for ground state and metastable He. Note that the metastable cross section displayed in figure 3.6 is multiplied by 0.01, therefore the cross sections become equal at about 70 keV/amu. At about 1 keV/amu the metastable cross section exceeds the ground state one by not less than four orders of magnitude. This arises from the fact that capture from the metastables can almost resonantly populate the $He^+(n = 4)$ levels, while capture from ground state He has to overcome a large endothermic energy defect.

The large difference between the metastable

and ground state He cross sections can have severe implications for plasma diagnostics. Note that an abundance of 1% of metastable neutrals in a cold region of the plasma (temperatures corresponding to collision energies below 5 keV/amu) implies that the HeII($n = 4 \rightarrow n = 3$) line emission is dominated by capture from metastables. For collisions with the 45 keV/amu He heating beams at JET, which contain metastable He fractions on the percentage level (Summers *et al.* [9]), capture from the metastable component may contribute some 20 to 30% to the observed signals. This is a significant correction for accurate local CXS diagnostics (see e.g. von Hellermann *et al.* [8]). In this context it is noteworthy that in Japan at the JT-60 Tokamak metastable fractions of 20% have been reported (Tobita *et al.* 1990 [44]).

3.6 Conclusion

Electronic redistribution processes in collisions of He^{2+} ions with neutral helium atoms have been studied by means of Photon Emission Spectroscopy. The crossed beam experiments have been performed in the energy range of 1 to 75 keV/amu, encompassing the energies of present day He heating and diagnostics beams at large tokamaks. We have identified two channels contributing to the He^{1+} line emission namely pure one-electron capture (process (i)) and simultaneous electron removal and target-ion excitation (processes (ii) and (iii)). Due to the symmetry of the system and the large exo- and endothermicity of the one-electron capture channels these processes, electron capture and target-ion excitation, are equally strong at energies below approximately 10 keV/amu. The experimental results are confirmed by atomic-orbital calculations [30]. We argue that the fact that both processes are equally likely can be expected from the quasi-molecular picture of slow collisions. The equality of the cross sections of both HeII($n = 4 \longrightarrow n = 3$) production processes can also be understood within the framework of the classical overbarrier model.

Four-body Classical Trajectory Monte Carlo calculations were performed by Meng and Olson in the energy range of 50 to 300 keV/amu. In the energy range where experiment and theory overlap there is in general fair agreement, although the l distributions within a principal quantum shell exhibit differences, the high l states being underestimated by theory. The total n shell cross sections seem to provide a basis for plasma diagnostics in the intermediate energy range. He plasma ions with such energies have been observed in large tokamaks as TFTR and JET.

By using all the experimental and theoretical data we have determined a reliable cross section data base that is needed for neutral helium beam based plasma diagnostics on large tokamaks. However we have indicated that metastable He atoms may have a large impact on Charge Exchange Spectroscopy based on the HeII($n = 4 \rightarrow n = 3$) line emission in the visible spectral range around 468.6 nm.